Thin–Walled Structures 214 (2025) 113357

Contents lists available at ScienceDirect

Thin-Walled Structures

journal homepage: www.elsevier.com/locate/tws

Full length article

A semi-analytical model elaborates the effect of cohesive zone on the peeling behaviors of heterogeneous thin films

Bingzhan Zhu [a], Kun Geng [a], Hao Li [a], Zuoqi Zhang [a,b,*]

[a] Department of Engineering Mechanics, School of Civil Engineering, Wuhan University, Wuhan, 430072, China
[b] Engineering Research Center on Building Examination and Reinforcement Technology (Ministry of Education), Wuhan University, Wuhan, 430071, China

ARTICLE INFO

Keywords:
Directional adhesion
Peeling
Cohesive zone
Heterogeneity
Bio-inspired design

ABSTRACT

Film-substrate systems are prevalent in various industries, and manipulation of their adhesion strength is essential to guarantee their desired functionalities. Inspired by the heterogeneous characteristic of geckos' spatulae, heterogeneous adhesion devices are proposed for enhanced directional adhesion, but experimental measurements of their adhesion strength are significantly lower than the theoretical predictions. This discrepancy is likely due to the cohesive zone, a factor that was usually overlooked in previous theoretical models. To elucidate the effects of the cohesive zone on the peeling behavior of bio-inspired heterogeneous thin films, we developed a semi-analytical model based on energy principles. In the model, the peeling force can be determined by two dimensionless parameters: the heterogeneity factor and the cohesive-zone factor. The heterogeneity factor significantly strengthens the adhesion when peeling from the soft side to the stiff side, and weakens the adhesion when peeling from the opposite direction. This indicates that heterogeneity simultaneously facilitates the attachment in soft-stiff direction and the detachment in stiff-soft direction. The cohesive-zone factor partially offsets the attachment enhancement by heterogeneity; however, the cohesive-zone factor has marginal impact on the detachment enhancement. This study systematically reveals the combined effects of heterogeneity and cohesive zone on the peeling behaviors of bio-inspired heterogeneous thin films and provides useful guidelines for the design of smart attachment/detachment adhesion systems.

1. Introduction

Film-substrate systems are widely utilized in numerous industries, including micro-electromechanical systems (MEMS) [1], locomotion robotics [2], and advanced manufacturing [3,4]. The ability to precisely design and manipulate film/substrate adhesion is essential for various functional applications [5–7]. Nature offers a number of biological adhesion systems that exhibit swift and smart control in adhesion. Notably, the adhesion system of geckos serves as an exemplary model for the designs of functional adhesive devices. The average stress between a gecko's feet and contacted surfaces can reach up to 100 N/cm^2 (~10 atm) [8,9]. Despite such a strong attachment, geckos can detach effortlessly from and climb rapidly on diverse surfaces. This combination of two seemingly contradictory properties, strong attachment and easy detachment, is elegantly realized within geckos' adhesion systems. Previous investigations have revealed that the geckos' adhesion is the van der Waals force in nature [10,11], which is universal yet weak intermolecular forces; however, geckos achieve remarkably reversible adhesion through their hierarchical brush-like fiber array system.

Fig. 1(a) illustrates the typical hierarchical structure of the geckos' adhesion system [12,13]. The gecko toes are covered with lamellar forms of seta array, and each seta further branches into hundreds of spatulae at the tip. Significant research efforts have focused on elucidating the adhesion mechanisms of geckos through theoretical modeling, computational simulations, and experimental demonstrations. For instance, Geim et al. [9] manufactured adhesives mimicking gecko spatulae using arrays of submicrometric polyimide pillars. Their work demonstrated that such gecko-like adhesives can achieve an adhesion strength of 3 N/cm^2 (~0.3 atm) when the pillars are designed with appropriate density and geometry. In contrast, the unstructured polyimide films exhibited a negligible adhesion strength ($<10^{-3}$ N/cm^2), underscoring the importance of spatula design in the adhesion behaviors. Gao et al. [12] modeled the spatula as an elastic cylinder with a flat tip in contact with semi-infinite substrates, and found that the nano-scale size of spatulae is crucial for achieving high adhesion strength and tolerating potential contact flaws. Yao et al. [14] further

* Corresponding author.
E-mail address: zhang_zuoqi@whu.edu.cn (Z. Zhang).

https://doi.org/10.1016/j.tws.2025.113357
Received 3 March 2025; Received in revised form 18 April 2025; Accepted 21 April 2025
Available online 22 April 2025

proposed a bottom-up design of hierarchical structures mimicking geckos' spatula array, and demonstrated that the work of adhesion and flaw-tolerant size both exponentially increase with the number of hierarchy levels. Although these studies confirmed the significance of spatulae in realizing strong adhesion, the mechanism of easy detachment has been mainly attributed to the asymmetry of setae at a larger scale (the setae generally feature an inclination angle ~30° not 90° with the contacted surfaces) [12]. However, the specific characteristics of spatulae in geometry and material have not been paid much attention. Actually, many organisms that have adhesion-based locomotion systems possess spatula-like terminal elements [15]. Fig. 1(b) highlights these similarities, emphasizing the significance of spatula-like structures in adhesion. It is essential to recognize that the spatulae in contact with a substrate function more like elastic thin films [13], rather than simple micropillars.

Considering the spatula as an elastic thin film facilitates understanding the mechanics involved in the terminal adhesive element contacting with substrates. Tian et al. [13] established a theoretical model for peeling a thin film from a substrate based on force balances, to account for the friction and adhesion mechanisms in geckos' toe attachment and detachment. They suggested that the transition between attachment and detachment may be controlled by the toe's rolling motion that alters the peeling angle. Chen et al. [16] developed a hierarchical model covering multiple levels from the spatula to the toe. Their findings indicated that the specific geometry of spatula allows for a relatively large contact area with surfaces and so achieve the maximal adhesion strength even with discontinuous contact. They further employed the classical Kendall model [17] to show that the peeling force could be increased approximately tenfold at the spatula level by optimizing the spatula angle. Recent progresses in this field have presented various peeling models to study the effects of the thin film length [18,19], bending stiffness [20], heterogeneity [21–25], and pretension [26], as well as the film-substrate periodic cohesive interactions [27] and cohesive zone [28,29]. These factors generally fall into two categories: film properties and film-substrate interaction properties. The effect of heterogeneity in composite interfaces had been studied in Kendall's work on controlling the interface cracks [30]. The inverted triangle tip of the gecko's spatulae reflects their evident heterogeneity in geometry [31], as shown in Fig. 1(a); as a result, there must be heterogeneity in the bending stiffness. Xia et al. [21] theoretically investigated the effect of stiffness heterogeneity on peeling of a thin film from a substrate, and found that the heterogeneity would significantly increase the critical peeling force when peeling from the low stiffness segment to the high stiffness segment, whereas it would decrease the critical peeling force when peeling in the other direction. In another word, the heterogeneity surprisingly enhances the directionality in adhesion, simultaneously making the attachment stronger in one direction and the detachment easier in the other direction. However, the experimental measurements of the attachment force distinctly fell below the theoretical predictions. This may be mainly attributed to the effect of cohesive zone that was not taken into account in the theoretical models. Avellar et al. [28] carried out experiments and finite element simulations to investigate the effect of cohesive zones on the peeling behaviors of heterogeneous adhesive tapes, and indicated that the existence of cohesive zones suppress the adhesion enhancement by the bending stiffness heterogeneity. In natural biological adhesion systems such as the geckos', the spatula-like terminal elements of adhesion have such a small size up to tens of nanometer, comparable to the action range of van der Waals forces, and hence the cohesive zone effect is likely non-negligible. Therefore, a critical question arises, how the cohesive zone and structure heterogeneity interplay to define the directional peeling behaviors of the biological or bioinspired adhesion systems.

To clarify the interplaying mechanisms between cohesive zone and structural heterogeneity in the film-substrate systems, here we establish a theoretical peeling model for a heterogeneous thin film attached to a rigid substrate with the cohesive zone taken into account. In the model, the potential energy for the whole system, especially including the cohesive energy in the cohesive zone, was established, and a semi-analytical solution of the peeling force was derived based on the principle of minimum potential energy. Interestingly, the peeling force can be characterized with two dimensionless parameters: the cohesive-zone factor and the heterogeneity factor, respectively representing the effect of cohesive zone and structure heterogeneity as their names indicate. For verification purposes, extensive finite element simulations were conducted to complement the theoretical predictions.

2. Theoretical model

The peeling model for a heterogeneous film on a rigid substrate, which incorporates the cohesive zone, is illustrated in Fig. 1(c). The film is composed of two segments, designated as Segment 1 and Segment 2. The film is treated as a beam in a plane-strain state. The bending stiffnesses of Segment 1 and 2 are denoted by $D_1^* = E_1^* I_1^*$ and $D_2^* = E_2^* I_2^*$, respectively. Here, $E_i^* (i = 1, 2)$ is the plane strain modulus, defined as

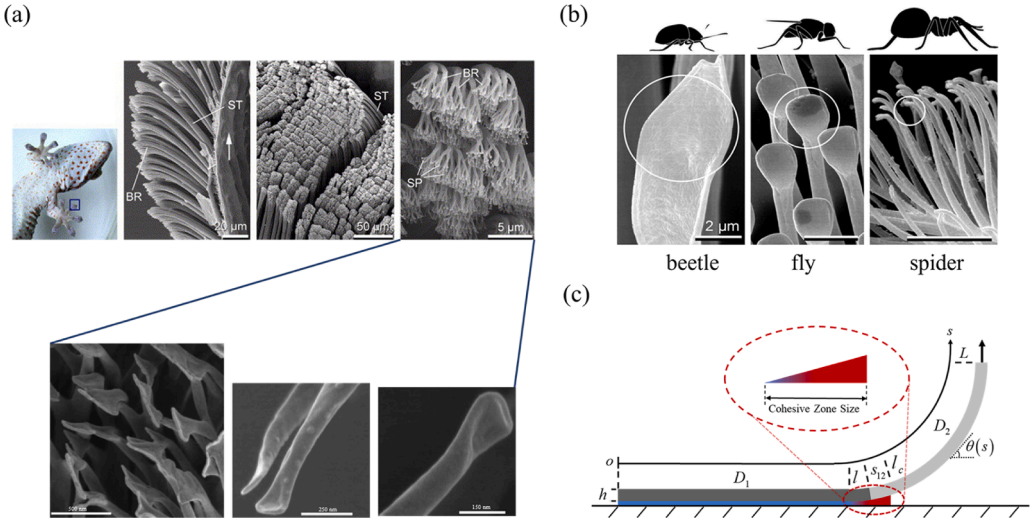

Fig. 1. (a) The hierarchical structures of gecko's adhesive system [12], with the spatula as its terminal element [30]; (b) Non-uniform structure designs of spatula-like adhesive elements seen in some insects [15]; (c) The mechanical model of a two-segment thin film attached to a rigid substrate, in which the two segments have different bending stiffness and especially the cohesive zone is taken into account.

$E_i/(1-\nu_i^2)$, in which E_i is the elastic modulus and ν_i is the Poisson's ratio. $I_i^*(i=1,2)$ denotes the moment of inertia of the cross-section per unit width, calculated as $h_i^3/12$ with h_i being the film thickness. Structure heterogeneity can arise from the variations in E_i^* or/and I_i^*. The film is assumed to be inextensible, which is valid at large peeling angles. During the peeling process, the heterogeneous film is peeled vertically off the substrate, gradually from Segment 2 to Segment 1, in which a cohesive zone of a certain size is especially included instead of the ideal brittle debonding point. The cohesive zone is modeled as a triangular region, at the front of which the film is perfectly adhered to the substrate while completely deboned from the substrate at the rear. For analytical convenience, a curvilinear coordinate system (s,θ) is introduced to describe the deformation of the film with the function $\theta(s)$. Here, s denotes the arc-length of the film measured from the origin o at the left end, while θ represents the inclination angle between the tangent to the film and the horizontal axis. The arc coordinates l and l_c denote the front and rear end of the cohesive zone, respectively, while L represents the total length of the heterogeneous film.

The traction-separation relationship within the cohesive zone is assumed to be a bilinear curve [32], fully defined by three key parameters: the peak stress σ_p, critical separation δ_c, and interface energy γ. Given the nature of peeling at large angles, it is reasonable to consider only normal interfacial traction [17]. Thus, the cohesive law is expressed as follows:

$$\sigma=\begin{cases}\dfrac{\delta}{\delta_p}\sigma_p & 0\le\delta\le\delta_p\\ \dfrac{\delta_c-\delta}{\delta_c-\delta_p}\sigma_p & \delta_p\le\delta\le\delta_c\end{cases} \tag{1}$$

where δ_p represents the separation corresponding to the peak stress σ_p, and denote $\alpha=\delta_p/\delta_c$. The interface energy γ can be calculated as:

$$\gamma=\frac{1}{2}\delta_c\sigma_s \tag{2}$$

Under steady-state peeling conditions for homogeneous materials, the cohesive zone size remains constant and can be approximated as follows [16,33,34]:

$$c_i=\left(\frac{E_i^*h_i^3\gamma}{\sigma_p^2}\right)^{\frac{1}{4}}=\left(\frac{12D_i^*\gamma}{\sigma_p^2}\right)^{\frac{1}{4}}=\left(\frac{3D_i^*\delta_c^2}{\gamma}\right)^{\frac{1}{4}} \tag{3}$$

For heterogeneous materials composed of two segments, the cohesive zone size changes as peeling transitions from Segment 2 to Segment 1 [28]. However, the details of this change is still unknown to a large extent. According to the physical peeling process, there should be three stages. In Stage 1, steady-state peeling occurs in Segment 2, and hence the cohesive zone size is a constant, equivalent to that for the homogeneous film of Segment 2. In Stage 2, transitional peeling happens with the cohesive zone spanning both Segment 2 and Segment 1, and therefore the cohesive zone size changes as the peeling propagates. In Stage 3, steady-state peeling occurs in Segment 1, and the cohesive zone size keeps a constant as that for the homogeneous film of Segment 1, with analogy to Stage 1. Evidently, Stages 1 and 3 are just the same as the peeling process of homogeneous films, and the cohesive zone does not change and makes no effects under the steady peeling scenario considered here. For Stage 2, the cohesive zone comes into play; for the simplicity of theoretical modeling, a linearly varying form of the cohesive zone size is assumed as the peeling front propagates in Stage 2, illustrated in Fig. 2. Mathematically, the cohesive zone size can be defined as the following function of the length l:

$$c(l)=\begin{cases}c_2 & s_{12}<l\le L\\ \dfrac{c_1-c_2}{c_1}\cdot(s_{12}-l)+c_2 & s_{12}-c_1<l\le s_{12}\\ c_1 & 0\le l\le s_{12}-c_1\end{cases} \tag{4}$$

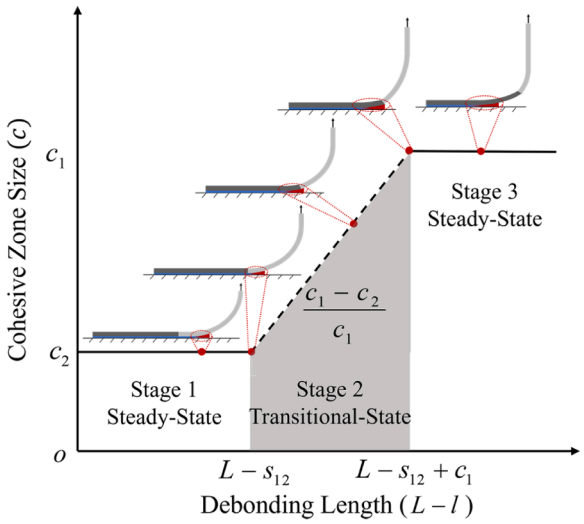

Fig. 2. Illustration of the cohesive zone size variation as the detachment going to the segment 1 from the segment 2.

where s_{12} represents the arc coordinate at the interface between the two segments, c_1 and c_2 denote the cohesive zone size in Segment 1 (Stage 3) and Segment 2 (Stage 1), respectively.

As illustrated in Fig. 3, the cohesive energy in the cohesive zone can be integrated from the traction-separation curve:

$$\prod_{cohesive}=-\left[\int_l^{l_0}\left(\gamma-\frac{\delta^2\sigma_p}{2\delta_p}\right)ds+\int_{l_0}^{l_c}\frac{(\delta_c-\delta)^2\sigma_p}{2(\delta_c-\delta_p)}ds\right] \tag{5}$$

where l_p corresponds to the arc coordinate at peak stress. Considering the triangular configuration of the cohesive zone, the cohesive energy can be simplified to be:

$$\prod_{cohesive}=-\frac{1+\alpha}{3}\int_l^{l_c}\gamma ds \tag{6}$$

Consequently, the total potential energy of the system can be formulated as:

$$\Pi=\int_l^{s_{12}}\frac{1}{2}D_1\theta'^2ds+\int_{s_{12}}^{L}\frac{1}{2}D_2\theta'^2ds-F\int_0^L\sin\theta ds-\int_0^l\gamma ds-\frac{1+\alpha}{3}\int_l^{l_c}\gamma ds \tag{7}$$

where θ' is the first derivative of θ with respect to the arc coordinate s, the first and second terms represent bending strain energy, the third term represents external force potential energy, the fourth term represents interface energy, and the last term represents the interface energy in the cohesive zone.

Applying the principle of minimum potential energy, we get that the variation of the total potential energy with respect to l and θ is equal to zero:

$$\delta\Pi=\frac{\partial\Pi}{\partial l}\delta l+\frac{\partial\Pi}{\partial\theta}\delta\theta=0 \tag{8}$$

Combine the boundary condition ($\theta(l)=0,\theta'(L)=0$) and the continuity of bending moment ($M|_{s_{12}^-}=M|_{s_{12}^+}$), we can derive:

$$\begin{aligned}&D_1\theta''+F\cos\theta=0\\ &D_2\theta''+F\cos\theta=0\\ &\frac{1}{2}D_1\theta_l'^2-\gamma-\frac{1+\alpha}{3}\gamma c'_l=0\\ &D_1\theta'|_{s_{12}^-}-D_2\theta'|_{s_{12}^+}=0\\ &\theta'_L=0\end{aligned} \tag{9}$$

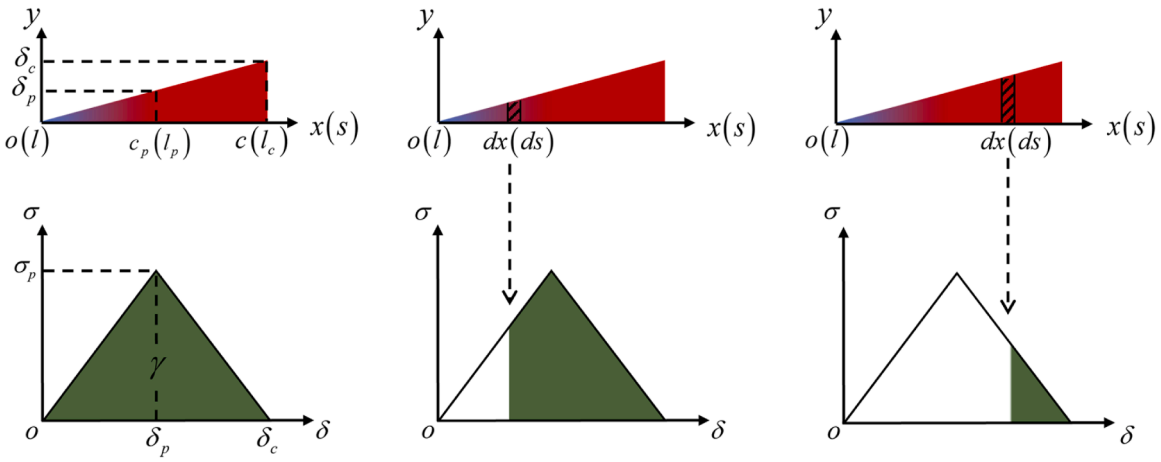

Fig. 3. Illustration of the calculation of the cohesive energy.

where θ'' is the second derivative of θ with respect to l, and

$$c_l' = m\frac{\mathrm{d}c}{\mathrm{d}l} = -m\cdot\frac{c_1 - c_2}{c_1} = -m\cdot\left[1 - \left(\frac{D_1}{D_2}\right)^{-\frac{1}{4}}\right] \tag{10}$$

here m is a correction coefficient introduced to compensate for the simplified linear hypothesis of cohesive zone size change across the interface (Stage 2 shown in Fig. 2), since the actual variation of the cohesive zone size should be more complex, depending on many factors, such as γ, δ_c, α, and D_2. Based on dimensional analysis of mechanics, the dimensionless coefficient is inferred to be a function of two dimensionless factors as below:

$$m\left(\left(\frac{D_2}{\gamma\delta_c^2}\right)^{\frac{1}{4}}, \alpha\right) \tag{11}$$

Combing Eqs. (3) and (4), it can be inferred with ease that the first dimensionless parameter actually represents the normalized cohesive zone size c_2 in the following way:

$$\left(\frac{D_2}{\gamma\delta_c^2}\right)^{\frac{1}{4}} \sim \left(\frac{3D_i\delta_c^2}{\gamma}\right)^{\frac{1}{4}} \Big/ \delta_c \sim c_2 / \delta_c \tag{12}$$

Then, the peeling force can be solved to be (See Appendix for the derivation in detail):

$$F = \frac{D_1\gamma\cdot\left(1 + \frac{1+\alpha}{3}\cdot c_l'\right)}{D_2 + (D_1 - D_2)\sin\theta_{s_{12}}} \tag{13}$$

Without loss of generality, here we assume $D_1 > D_2$. Considering the small bending deformation of the thin film over the cohesive zone, we can set $\theta_{12} = 0$ and get a maximum value of the peeling force:

$$F_{\max}^{21} = \frac{D_1\gamma}{D_2}\cdot\left(1 + \frac{1+\alpha}{3}\cdot c_l'\right) = \frac{D_1\gamma}{D_2}\cdot\left\{1 - \frac{1+\alpha}{3}\cdot m\cdot\left[1 - \left(\frac{D_1}{D_2}\right)^{-\frac{1}{4}}\right]\right\} \tag{14}$$

Similarly, if peeling from the other direction (i.e., from Segment 1 to Segment 2), we can derive a minimum value of the peeling force:

$$F_{\min}^{12} = \frac{D_2\gamma}{D_1}\cdot\left(1 + \frac{1+\alpha}{3}\cdot c_l'\right) = \frac{D_2\gamma}{D_1}\cdot\left\{1 - \frac{1+\alpha}{3}\cdot m\cdot\left[1 - \left(\frac{D_2}{D_1}\right)^{-\frac{1}{4}}\right]\right\} \tag{15}$$

We can see that $F_{\max}^{21}$ and $F_{\min}^{12}$, respectively, represent the strong attachment force and the weak detachment force in the directional behaviors of the gecko-inspired adhesion structure. In the equations above, the coefficients $(1+\alpha)/3$ and m both are related to the cohesive zone, and m is also a function of α, and so we combine them into a new dimensionless parameter M as below:

$$M = \frac{1+\alpha}{3}\cdot m = M\left(\alpha,\ \left(\frac{D_2}{\gamma\delta_c^2}\right)^{\frac{1}{4}}\right) \tag{16}$$

M is supposed to be a function of $\left[D_2/\left(\gamma\delta_c^2\right)\right]^{1/4}$ and α. It is difficult to analytically derive the specific expression of M, and hence we turn to seek a semi-empirical solution based on finite element analysis (FEA) in the following section. Noteworthy that the differential equations in Eq. (9) can also be solved via some numerical methods, e.g., the shooting method as done in previous works [18–20,22]. However, an analytical solution is highly desirable, since analytical solutions have incomparable advantage of numerical solutions in unveiling the fundamental law and mechanism in principle.

Finally, the peeling forces in Eqs. (14) and (15) can be expressed in a more concise format as below:

$$\frac{F_{\max}^{21}}{\gamma} = \frac{D_1}{D_2}\cdot\left\{1 - M\cdot\left[1 - \left(\frac{D_1}{D_2}\right)^{-\frac{1}{4}}\right]\right\} \tag{17}$$

$$\frac{F_{\min}^{12}}{\gamma} = \frac{D_2}{D_1}\cdot\left\{1 - M\cdot\left[1 - \left(\frac{D_2}{D_1}\right)^{-\frac{1}{4}}\right]\right\} \tag{18}$$

Here, the physical meaning of every term is quite self-evident: (1) the bending stiffness ratio outside the brace (e.g., D_1/D_2) represents the enhancing effect of structural heterogeneity; (2) the ratio in the braces (e.g., $M\cdot\left[1 - (D_1/D_2)^{-1/4}\right]$) denotes the weakening effect due to the cohesive zone. When $D_1 = D_2$, Eqs. (17) and (18) yield $F_{\max}^{21} = F_{\min}^{12} = \gamma$, corresponding to the analytical solution for homogeneous films. For heterogeneous films $(D_1 > D_2)$, if the effect of cohesive zone is not taken into consideration, the equations go back to $F_{\max}^{21} = (D_1/D_2)\gamma$ and $F_{\min}^{12} = (D_2/D_1)\gamma$, respectively, just the same as the solutions by Xia et al. [21]; if the cohesive zone effect is considered, Eqs. (17) and (18) clearly suggest that the effect of structural heterogeneity would be offset to some extent.

3. Results and discussion

In order to validate our theoretical model and systematically investigate the effect of cohesive zone, we conducted FEM simulations with ABAQUS 2016. In the FEM models, the plain strain element CPE4 was adopted for the heterogeneous film, an analytical rigid body was used to simulate the substrate, and the cohesive element COH2D4 was employed to model the interaction between the film and the rigid substrate. The substrate was always fixed, while a vertical displacement was applied to the right end of the film. The non-bonded part of the film was sufficiently long to achieve 90° peeling. Before conducting systematic simulations, mesh convergence analyses were performed on the FEM model to ensure the simulation results are consistent and reliable.

The bilinear cohesive law (see Fig. 3) adopted in the simulations have three independent parameters. Hereafter, the interface energy γ, and the separation displacement δ_c, and the separation ratio α are adopted to characterize the cohesive law. Noteworthy that α is inversely related to the interface stiffness (the initial slope of the cohesive curve), while γ and δ_c are fixed. Hence, α is sometimes referred as the interface stiffness hereafter. For convenience, the following group of parameter values are adopted as base reference:

$\gamma_0 = 0.01\ \mathrm{J{\cdot}m^{-2}}$;
$\delta_{c0} = 1\ \mathrm{nm}$;
$\nu = 0.3$;
$h_0 = 5\ \mathrm{nm}$;
$E_0 = 1\ \mathrm{GPa}$;
$E_0^* = 1/(1-\nu^2) = 1.0989\mathrm{GPa}$;
$D_0^* = E_0^* h_0^3/12 = 11.4469\mathrm{nN{\cdot}nm}$

Fig. 4(a) shows the plots of the cohesive zone size and peeling force varying with respect to the debonding length. At the onset of peeling, the cohesive zone size increases linearly from 0 to a steady-state value of Segment 2, and correspondingly the peeling force rises non-linearly from 0 to its steady-state value. Then, the peeling process goes into Stage 1, as aforementioned in Fig. 2. As the cohesive zone approaches the interface between Segment 1 and 2, the peeling process goes into Stage 2. In this stage, the peeling force rises quickly to a high peak far beyond the steady value of the homogeneous segment; the cohesive zone size generally increases from c_2 (for homogeneous Segment 2) to c_1 (for homogeneous Segment 1) in a linear way as assumed in our theoretical model, see Fig. 4(b). However, the FEM simulation results clearly present that the cohesive zone size has a slight drop below c_2 at the beginning of Stage 2, and then increases quickly to reach a peak beyond c_1. These localized details reflect the mechanical complexity of the transitional stage when the cohesive zone crosses the interface between Segment 1 and 2, and the deviation from a simply linear transition from c_2 to c_1 in cohesive zone size also justify the necessity of the introduction of the correction coefficient m. As the cohesive zone passes the interface and enters Segment 1, the peeling force gradually decreases to a steady value of the homogeneous segment, and the cohesive zone size also slightly decreases to c_1. Then, the peeling process goes into Stage 3, another steady peeling stage similar to Stage 1.

To check the influences of the separation ratio α and the film bending stiffness D on the cohesive zone size, Fig. 5 shows the variations of cohesive zone size for different α and D under the condition that the interface energy γ and critical separation displacement δ_c are kept to be constant. It can be seen that the cohesive zone size is independent of α (i.e., the interface stiffness here), but increases with the film bending stiffness D, well consistent with the theoretical prediction by Eq. (3). To ascertain the specific form of the coefficient function $M\left(\alpha, \left[D_2/\left(\gamma\delta_c^2\right)\right]^{1/4}\right)$, we investigated the influences of the two variables on the peeling force through checking FEM simulation results. Fig. 6

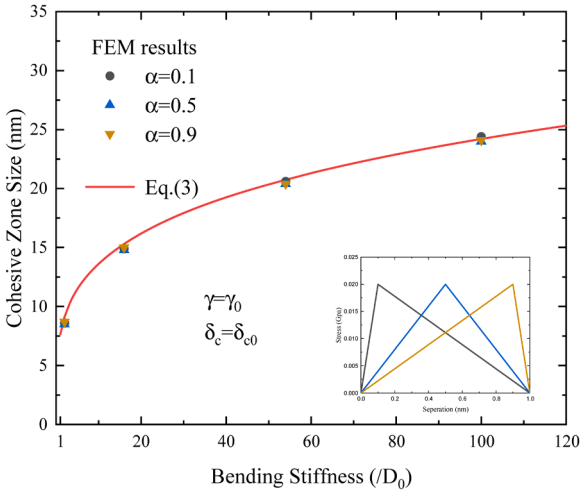

Fig. 5. Variations of the cohesive zone size for different D and α, with the interface energy γ and the critical separation displacement δ_c fixed.

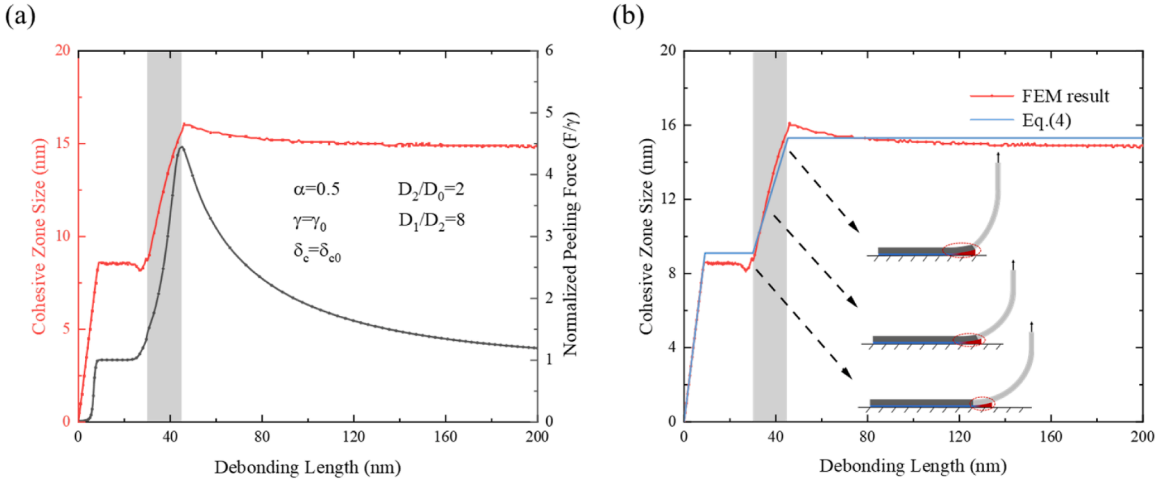

Fig. 4. FEM-based verification of the linearly varying form of the cohesive zone size with respect to the debonding length around the interface: (a) the normalized peeling force and cohesive zone size co-vary with respect to the debonding length; (b) the determination of the varying rate of cohesive zone size around the interface.

presents the plots of the normalized maximum peeling force against the bending stiffness ratio D_1/D_2 for different α and D_2 under the condition that the interface energy γ and critical separation displacement δ_c are kept to be constant. Three points can be figured out from the plots: (1) the peeling force is always equal to the interface energy when $D_1/D_2 = 1$ (i.e., the homogeneous case), regardless of α and D_2; (2) the maximum peeling force significantly increases with the bending stiffness ratio (D_1/D_2) as well as the film bending stiffness of Segment 2 (D_2); (3) most interestingly, α shows negligible effect on the maximum peeling force, and M can be further simplified to be a function of the sole variable $\left[D_2/\left(\gamma\delta_c^2\right)\right]^{1/4}$. Regarding the role of the interface stiffness (α), studies on the cohesive interface in composites have obtained similar conclusions [33]. They suggested that either two of the three parameters, the interface energy, the cohesive strength, and the critical separation displacement, are most critical for using a bilinear cohesive law to simulate the interface delamination. Thus, without loss of generality, α is always set to be 0.5 in the subsequent simulations, unless otherwise specified.

Extensive FEM calculations were carried out on a series of combinations of interface energy, critical separation displacement, and bending stiffness, as listed in Table 1. For each combination $\left[D_2/\left(\gamma\delta_c^2\right)\right]^{1/4}$, eight cases of different bending stiffness ratios were simulated via FEM to calculate their maximum peeling forces, and further to determine the corresponding correction coefficient M by fitting. Finally, a series of M corresponding to these combinations $\left[D_2/\left(\gamma\delta_c^2\right)\right]^{1/4}$ were obtained, as shown in Fig. 7. By fitting these data, the expression for the correction coefficient M can be acquired to be:

$$M = 0.4252 + 0.9896\cdot\exp\left(-\left(\frac{D_2}{\gamma\delta_c^2}\right)^{\frac{1}{4}}\Big/30.4645\right) \tag{19}$$

Hence, a semi-analytical solution for the maximum peeling force in Eq. (17) can be explicitly expressed as:

$$\frac{F_{\max}^{21}}{\gamma} = \frac{D_1}{D_2}\left\{1 - \left[0.4252 + 0.9896\cdot\exp\left(-\left(\frac{D_2}{\gamma\delta_c^2}\right)^{\frac{1}{4}}\Big/30.4645\right)\right]\cdot\left[1-\left(\frac{D_1}{D_2}\right)^{-\frac{1}{4}}\right]\right\} \tag{20}$$

It clearly indicates that the maximum peeling force is mainly determined by two dimensionless combinational parameters: D_1/D_2 and $\left[D_2/\left(\gamma\delta_c^2\right)\right]^{1/4}$. As aforementioned, the former parameter represents the film bending stiffness ratio between Segment 1 and Segment 2, while the latter parameter is a normalized cohesive zone size c_2/δ_c, and thus we name them as the heterogeneity factor and the cohesive-zone factor, respectively. Similarly, the semi-analytical solution for the minimum peeling force in Eq. (18) can be explicitly expressed as:

$$\frac{F_{\min}^{12}}{\gamma} = \left(\frac{D_1}{D_2}\right)^{-1}\cdot\left\{1 - \left[0.4252 + 0.9896\cdot\exp\left(-\left(\frac{D_2}{\gamma\delta_c^2}\right)^{\frac{1}{4}}\Big/30.4645\right)\right]\cdot\left[1-\left(\frac{D_1}{D_2}\right)^{\frac{1}{4}}\right]\right\} \tag{21}$$

It is interesting that Eq. (19) presents M as a monotonically decreasing function of $\left[D_2/\left(\gamma\delta_c^2\right)\right]^{1/4}$ and hence gives two extremums of M as $\left[D_2/\left(\gamma\delta_c^2\right)\right]^{1/4}$ approaches $+\infty$ and 0, respectively. If the film stiffness is extremely high or the cohesive strength is extremely low, i.e., $\left[D_2/\left(\gamma\delta_c^2\right)\right]^{1/4} = +\infty$, then Eq. (19) yields a minimum M, $M_{\min} = 0.4252$. Correspondingly, Eqs. (20) and (21) respectively become

$$\frac{F_{\max}^{21}}{\gamma} = \frac{D_1}{D_2}\left\{1 - 0.4252\cdot\left[1-\left(\frac{D_1}{D_2}\right)^{-\frac{1}{4}}\right]\right\} \tag{22}$$

$$\frac{F_{\min}^{12}}{\gamma} = \left(\frac{D_1}{D_2}\right)^{-1}\cdot\left\{1 - 0.4252\cdot\left[1-\left(\frac{D_1}{D_2}\right)^{\frac{1}{4}}\right]\right\} \tag{23}$$

The two equations above provide estimations on the weakest effect of cohesive zone on the maximum adhesion force and the minimum detachment force, respectively.

On the contrary, if the film stiffness is extremely low or the cohesive strength is extremely high, i.e., $\left[D_2/\left(\gamma\delta_c^2\right)\right]^{1/4} = 0$, then Eq. (19) gives a maximum M, $M_{\max} = 1.4148$. Consequently, Eqs. (20) and (21) lead to

$$\frac{F_{\max}^{21}}{\gamma} = \frac{D_1}{D_2}\left\{1 - 1.4148\cdot\left[1-\left(\frac{D_1}{D_2}\right)^{-\frac{1}{4}}\right]\right\} \tag{24}$$

$$\frac{F_{\min}^{12}}{\gamma} = \left(\frac{D_1}{D_2}\right)^{-1}\cdot\left\{1 - 1.4148\cdot\left[1-\left(\frac{D_1}{D_2}\right)^{\frac{1}{4}}\right]\right\} \tag{25}$$

Correspondingly, the two equations above represent the strongest effect of cohesive zone on the critical peeling forces.

In order to verify this semi-analytical solution, another eight combinations of interface energy, critical separation displacement, and Segment 2 bending stiffness were selected as listed in Table 2, and their FEM results of the maximum peeling force are shown in Fig. 8(a), along with the theoretical predicted curves. Note that the plots by Eqs. (22) and (24) are also included to show the possible weakest ($M_{\min} = 0.4252$) and strongest ($M_{\max} = 1.4148$) effects of cohesive zone on the maximum peeling force, respectively. First of all, we can see that the theoretical predictions are in good agreement with the FEM results, affirming the validity of our solution. As the bending stiffness ratio increases, the curves of maximum peeling force rise quite quickly, indicating stronger attachment achieved by the film heterogeneity. However, our predicted curves including the one of the weakest cohesive-zone effect ($M_{\min} = 0.4252$) are still much lower than the dash line ($F_{\max}^{21}/\gamma = D_1/D_2$) predicted by the model excluding the cohesive zone's effect. It is worth noting that M has a distinct influence on these curves. For the strongest case $M_{\max} = 1.4148$, one can see that the cohesive-zone effect is profound, and almost completely offset the heterogeneity effect. In another word, the previous studies that omitted the cohesive zone effect may distinctly overestimate the enhancement in

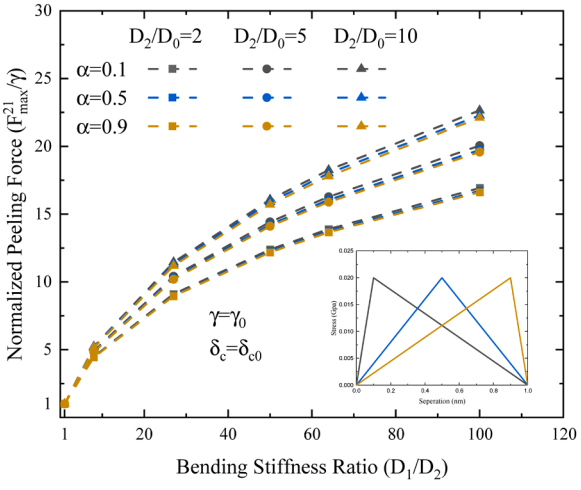

Fig. 6. Plots of the normalized maximum peeling force against the bending stiffness ratio for different $\alpha$from FEM simulations. Here the interface energy and the critical separation displacement are both fixed.

Table 1
Combinations of interface energy, critical separation displacement and bending stiffness used for FEM simulations to determine the coefficient function M.

Interface energy (γ)	Critical separation displacement(δ_c)	Bending stiffness (D_2)	Cohesive-zone factor $\left[D_2/\gamma\delta_c^2\right]^{1/4}$	Heterogeneity(D_1/D_2)
$0.1\cdot\gamma_0$	$0.2\cdot\delta_{c0}$	$64\cdot D_0$	65.4187	1,8,27,50,64,100
$0.1\cdot\gamma_0$	$0.2\cdot\delta_{c0}$	$0.64\cdot D_0$	20.6872	
$1\cdot\gamma_0$	$1\cdot\delta_{c0}$	$10\cdot D_0$	10.3436	
$1\cdot\gamma_0$	$1\cdot\delta_{c0}$	$5\cdot D_0$	8.6979	
$0.3\cdot\gamma_0$	$1\cdot\delta_{c0}$	$1\cdot D_0$	7.8594	
$0.2\cdot\gamma_0$	$1\cdot\delta_{c0}$	$0.5\cdot D_0$	7.3140	
$1\cdot\gamma_0$	$1\cdot\delta_{c0}$	$2\cdot D_0$	6.9172	
$0.1\cdot\gamma_0$	$1\cdot\delta_{c0}$	$0.1\cdot D_0$	5.8166	

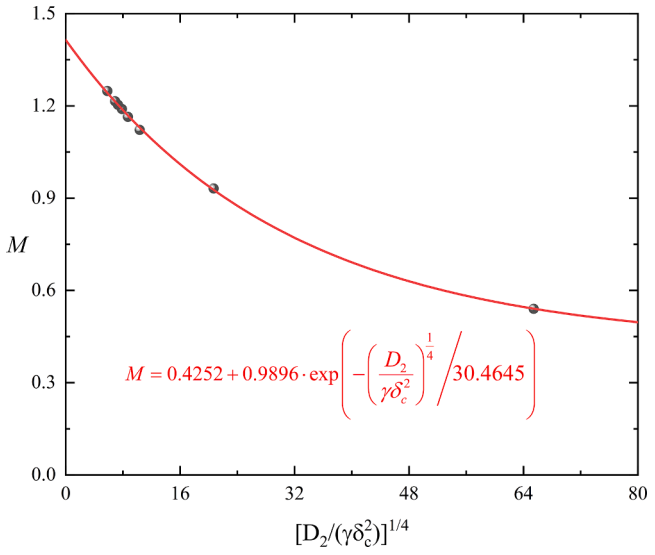

Fig. 7. Coefficient M obtained as a function of $\left[D_2/\left(\gamma\delta_c^2\right)\right]^{1/4}$ by fitting to FEM results (data points).

attachment by the heterogeneity. If we peel in the other direction, i.e., from the stiff Segment 1 to the soft Segment 2, we can just interchange D_1 and D_2 in Eq. (20) to obtain the minimum peeling force needed for detachment, as indicated by Eq. (21). Two theoretical predicted curves are shown in Fig. 8(b), together with the data points from FEM simulations (the parameters adopted listed in Table 3). In addition, the plots by Eqs. (23) and (25) are also included to show the possible weakest ($M_{\min} = 0.4252$) and strongest ($M_{\max} = 1.4148$) effects of cohesive zone on the minimum peeling force, respectively. The theoretical predictions agree well with the FEM results, and they both showed that the minimum peeling force decreases quickly with the bending stiffness ratio, indicating easier detachment achieved by the film heterogeneity. Interestingly, the plots for different values of M including $M_{\min} = 0.4252$ and $M_{\max} = 1.4148$ are quite close to one another, which suggests that M has trivial influence in this scenario. Nevertheless, our predicted curves including the one of the weakest cohesive-zone effect ($M_{\min} = 0.4252$) are above the dash line ($F_{\min}^{12}/\gamma = D_2/D_1$) predicted by the model excluding the cohesive zone's effect, that means a slight underestimation of the detachment force if the cohesive zone effect is omitted.

Moreover, combining Fig. 8(a) and (b) together, we can conclude that the structure heterogeneity simultaneously enhances the attachment in soft-stiff direction and the detachment in stiff-soft direction, providing an amazing directional characteristic to the film-substrate adhesion which is not only greatly useful in biological attachment systems like gecko's but also highly desired in many industries such as robotics. On the other hand, the cohesive zone exhibits a reverse effect, partially offsetting the attachment enhancement by heterogeneity; however, its impact on the detachment enhancement is marginal. These mechanisms unveiled here can well explain the discrepancy between existing theory and experimental observations [28]. To systematically clarify the influence of the heterogeneity factor and cohesive-zone factor, the maximum peeling force for attachment (i.e., peeling from Segment 2 to Segment 1) and the minimum peeling force for detachment (i.e., peeling from Segment 1 to Segment 2) are respectively shown as contours in Fig. 9(a) and (b). One can see that for the attachment direction, larger heterogeneity and cohesive-zone factors generally lead to larger critical attachment forces. Noteworthy that the influence of the cohesive-zone factor is more pronounced when the heterogeneity factor is larger. On the contrary, for the detachment direction, the larger is the heterogeneity factor, the smaller is the detachment force; however, the cohesive-zone factor has little effect on the detachment force. These contours can serve as useful guidelines for the design of smart adhesion devices based on film-substrate systems.

4. Conclusions

In this paper, we systematically investigated the peeling behavior of bio-inspired heterogeneous film, especially with the cohesive zone considered. Based on the principle of minimum potential energy and dimensional analysis, a semi-analytical solution of the critical peeling force was derived, as a function of two dimensionless parameters: the heterogeneity factor D_1/D_2 and the cohesive-zone factor $\left[D_2/\left(\gamma\delta_c^2\right)\right]^{1/4}$, respectively, representing the effects of the film heterogeneity and the cohesive zone. The following major conclusions were drawn:

Table 2
Different combinations of interface energy, critical separation displacement and bending stiffness in FEM simulations for the theory validation.

Interface energy (γ)	Critical separation displacement(δ_c)	Bending stiffness (D_2)	Cohesive-zone factor $\left[D_2/\gamma\delta_c^2\right]^{1/4}$	Heterogeneity(D_1/D_2)
$0.1\cdot\gamma_0$	$1\cdot\delta_{c0}$	$1\cdot D_0$	10.3436	1,8,27,50,64,100
$0.3\cdot\gamma_0$	$1\cdot\delta_{c0}$	$2\cdot D_0$	9.3465	
$0.2\cdot\gamma_0$	$1\cdot\delta_{c0}$	$1\cdot D_0$	8.6979	
$1\cdot\gamma_0$	$0.7017\cdot\delta_{c0}$	$2\cdot D_0$	8.2260	
$0.6\cdot\gamma_0$	$1\cdot\delta_{c0}$	$2\cdot D_0$	7.8594	
$0.8\cdot\gamma_0$	$1\cdot\delta_{c0}$	$2\cdot D_0$	7.3140	
$0.5\cdot\gamma_0$	$1\cdot\delta_{c0}$	$1\cdot D_0$	6.9172	
$1\cdot\gamma_0$	$1.4142\cdot\delta_{c0}$	$2\cdot D_0$	5.8166	

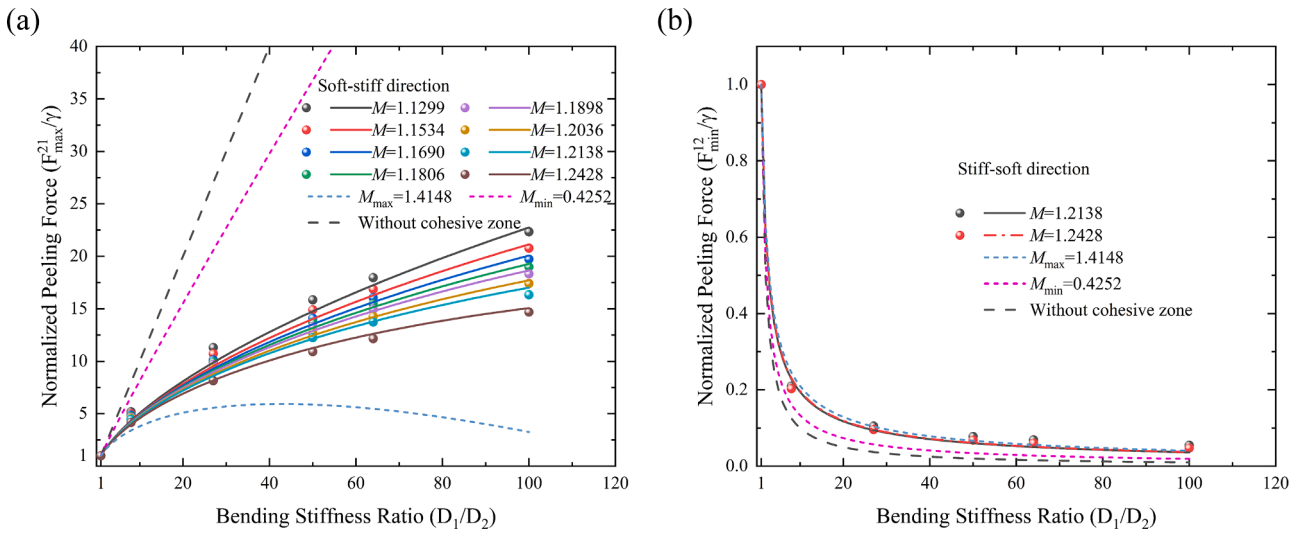

Fig. 8. Validation of the semi-analytical model with additional FEM simulation results: (a) Peeling from Segment 2 to Segment 1 (soft-stiff direction); (b) Peeling from Segment 1 to Segment 2 (stiff-soft direction).

Table 3
Different combinations of interface energy, critical separation displacement and bending stiffness in FEM simulations for the peeling in stiff-soft direction (from Segment 1 from Segment 2).

Interface energy (γ)	Critical separation displacement(δ_c)	Bending stiffness (D_2)	Cohesive-zone factor $\left[D_2/\gamma\delta_c^2\right]^{1/4}$	Heterogeneity(D_1/D_2)
$1\cdot\gamma_0$	$1\cdot\delta_{c0}$	$2\cdot D_0$	6.9172	1,8,27,50,64,100
$0.1\cdot\gamma_0$	$1\cdot\delta_{c0}$	$0.1\cdot D_0$	5.8166	

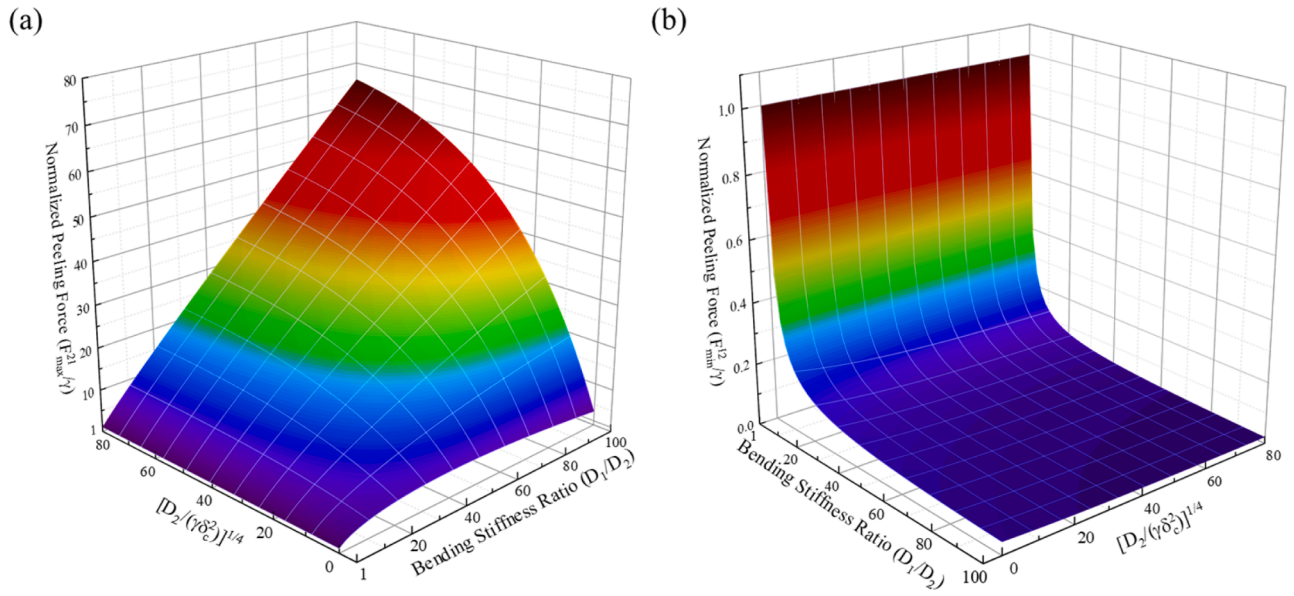

Fig. 9. Influence of the heterogeneity factor and cohesive-zone factor on the directional adhesion behaviors: (a) Contour of the attachment force, i.e., critical peeling force when peeling from Segment 2 to Segment 1; (b) Contour of the detachment force, i.e., critical peeling force when peeling from Segment 1 to Segment 2.

(1) Our model quantitatively clarifies the roles of structural heterogeneity and cohesive zone in the directional peeling behaviors of heterogeneous film-substrate systems. The model was well validated by comparing with FEM simulation results.
(2) The structural heterogeneity significantly enhances the adhesion when peeling from the soft side to the stiff side, and weakens the adhesion when peeling from the opposite direction. The heterogeneity induced directional characteristic simultaneously achieve strong attachment and easy detachment in a single design.
(3) The existence of cohesive zone partially offsets the attachment enhancement by heterogeneity; however, it has marginal impact on the detachment enhancement. A larger $\left[D_2/\left(\gamma\delta_c^2\right)\right]^{1/4}$ (corresponding to a smaller M) is suggested in the film-substrate system design to better reduce the unexpected effects of cohesive zones.

Our model explicitly elucidates the cohesive zone's effect on the heterogeneity-induced directional adhesion and provides valuable insights for the design of bio-inspired smart adhesion systems, as well as a deeper understanding of the reversible adhesion mechanisms employed by gecko-like biological systems. It is worth noting that our model is built on the basis of some simplifications, for instance, linear elastic materials, a bilinear cohesive law, 90° peeling, and small deformations within the cohesive zone. Further in-depth studies are certainly warranted, to cover aspects such as general materials, cohesive laws, and peeling angles, etc.

CRediT authorship contribution statement

Bingzhan Zhu: Writing – original draft, Validation, Methodology, Investigation, Conceptualization. **Kun Geng:** Validation. **Hao Li:** Validation. **Zuoqi Zhang:** Writing – review & editing, Writing – original draft, Supervision, Project administration, Methodology, Funding acquisition, Conceptualization.

Declaration of competing interest

The authors declare that they have no known competing financial interests or personal relationships that could have appeared to influence the work reported in this paper.

Acknowledgments

The work was supported by National Natural Science Foundation of China (Grant Nos. 12272279, 11720101002, 11772240), Key R&D Plan Projects of Hubei Province (No. 2021BCA106), and the Fundamental Research Funds for the Central Universities (2042024kf0034).

Appendix: Calculation of the critical peeling force

Taking the variation of total potential energy Eq. (7) with respect to l and θ:

$$\delta\Pi = -D_1\theta'_l|(\delta\theta)|_l + D_2\theta'_L(\delta\theta)|_L + \left(D_1\theta'|_{s_{12}^-} - D_2\theta'|_{s_{12}^+}\right)(\delta\theta)|_{s_{12}} - \int_l^{s_{12}} D_1\theta''\delta\theta ds - \int_{s_{12}}^{L} D_2\theta''\delta\theta ds - \frac{1}{2}D_1\theta_l'^2\delta l - \int_0^L F\cos\theta\delta\theta ds - \gamma\delta l - \frac{1+\alpha}{3}\gamma c'_l\delta l \tag{A1}$$

Considering the boundary conditions:$\theta(l) = 0, \theta'(L) = 0$, and noting that

$$\delta\theta(l) = (\delta\theta)|_l + \theta'|_l\delta l \tag{A2}$$

Eq. (A.1) can be further derived as

$$\delta\Pi = -\int_l^{s_{12}} (D_1\theta'' + F\cos\theta)\delta\theta ds - \int_{s_{12}}^{L} (D_2\theta'' + F\cos\theta)\delta\theta ds + \left[\frac{1}{2}D_1\theta_l'^2 - \gamma - \frac{1+\alpha}{3}\gamma c'_l\right]\delta l + \left(D_1\theta'|_{s_{12}^-} - D_2\theta'|_{s_{12}^+}\right)(\delta\theta)|_{s_{12}} + D_2\theta'_L(\delta\theta)|_L \tag{A3}$$

Eq. (8) requires that the terms before $\delta\theta$ and δl equal zero, and so we have:

$$D_1\theta'' + F\cos\theta = 0 \tag{A4}$$

$$D_2\theta'' + F\cos\theta = 0 \tag{A5}$$

$$\frac{1}{2}D_1\theta_l'^2 - \gamma - \frac{1+\alpha}{3}\gamma c'_l = 0 \tag{A6}$$

$$D_1\theta'|_{s_{12}^-} - D_2\theta'|_{s_{12}^+} = 0 \tag{A7}$$

$$\theta'_L = 0 \tag{A8}$$

Multiply Eq. (A4) by $D_1\theta'$ and then integrate from l to s_{12}^-, we obtain:

$$\frac{1}{2}D_1^2\left(\theta_l'^2 - \theta_{s_{12}^-}'^2\right) + FD_1(\sin\theta_l - \sin\theta_{s_{12}}) = 0 \tag{A9}$$

Similar operations apply to Eq. (A5), and we have:

$$\frac{1}{2}D_2^2\left(\theta_{s_{12}^+}'^2 - \theta_L'^2\right) + FD_2(\sin\theta_{s_{12}} - \sin\theta_L) = 0 \tag{A10}$$

Combing Eq. (A9) and Eq. (A10) together with Eqs. (A6–8), we get:

$$D_1\left[\gamma + \frac{1+\alpha}{3}\gamma c'_l\right] - FD_1\sin\theta_{s_{12}} + FD_2(\sin\theta_{s_{12}} - 1) = 0 \tag{A11}$$

Finally, we can obtain the formula of critical peeling force to be:

$$F = \frac{D_1\gamma\cdot\left[1 + \frac{1+\alpha}{3}\cdot c'_l\right]}{D_2 + (D_1 - D_2)\sin\theta_{s_{12}}} \tag{A12}$$

Data availability

No data was used for the research described in the article.

References

[1] Y. Fu, H. Du, W. Huang, S. Zhang, M. Hu, TiNi-based thin films in MEMS applications: a review, Sens. Actuators A: Phys. 112 (2004) 395–408.
[2] B. Chu, K. Jung, C.-S. Han, D. Hong, A survey of climbing robots: locomotion and adhesion, Int. J. Precis. Eng. Manuf. 11 (2010) 633–647.
[3] R. Hashemi Sanatgar, C. Campagne, V. Nierstrasz, Investigation of the adhesion properties of direct 3D printing of polymers and nanocomposites on textiles: effect of FDM printing process parameters, Appl. Surf. Sci. 403 (2017) 551–563.
[4] Z. Dai, L. Liu, Z. Zhang, Strain engineering of 2D materials: issues and opportunities at the interface, Adv. Mater. 31 (2019) 1805417.
[5] J.I. Yoo, S.H. Kim, H.C. Ko, Stick-and-play system based on interfacial adhesion control enhanced by micro/nanostructures, Nano Res. 14 (2021) 3143–3158.
[6] D.-G. Hwang, K. Trent, M.D. Bartlett, Kirigami-inspired structures for smart adhesion, ACS Appl. Mater. Interfaces 10 (2018) 6747–6754.
[7] H. Jiang, E.W. Hawkes, C. Fuller, M.A. Estrada, S.A. Suresh, N. Abcouwer, et al., A robotic device using gecko-inspired adhesives can grasp and manipulate large objects in microgravity, Sci. Robot. 2 (2017) eaan4545.
[8] K. Autumn, Y.A. Liang, S.T. Hsieh, W. Zesch, W.P. Chan, T.W. Kenny, et al., Adhesive force of a single gecko foot-hair, Nature 405 (2000) 681–685.
[9] A.K. Geim, S.V. Dubonos, I.V. Grigorieva, K.S. Novoselov, A.A. Zhukov, S. Y. Shapoval, Microfabricated adhesive mimicking gecko foot-hair, Nat. Mater. 2 (2003) 461–463.
[10] K. Autumn, A.M Peattie, Mechanisms of adhesion in geckos, Integr. Comp. Biol. 42 (2002) 1081–1090.
[11] K. Autumn, M. Sitti, Y.C.A. Liang, A.M. Peattie, W.R. Hansen, S. Sponberg, et al., Evidence for van der Waals adhesion in gecko setae, P. Natl Acad. Sci. USA 99 (2002) 12252–12256.
[12] H.J. Gao, X. Wang, H.M. Yao, S. Gorb, E. Arzt, Mechanics of hierarchical adhesion structures of geckos, Mech. Mater. 37 (2005) 275–285.
[13] Y. Tian, N. Pesika, H.B. Zeng, K. Rosenberg, B.X. Zhao, P. McGuiggan, et al., Adhesion and friction in gecko toe attachment and detachment, P. Natl Acad. Sci. USA 103 (2006) 19320–19325.
[14] H. Yao, H. Gao, Mechanics of robust and releasable adhesion in biology: bottom–up designed hierarchical structures of gecko, J. Mech. Phys. Solids 54 (2006) 1120–1146.
[15] E. Arzt, S. Gorb, R. Spolenak, From micro to nano contacts in biological attach devices, P. Natl Acad. Sci. USA 100 (2003) 10603–10606.
[16] B. Chen, P.D. Wu, H. Gao, Hierarchical modelling of attachment and detachment mechanisms of gecko toe adhesion, Proc. R. Soc. A-Math. Phys. Eng. Sci. 464 (2008) 1639–1652.
[17] K. Kendall, Thin-film peeling–the elastic term, J. Phys. D Appl. Phys. 8 (1975) 1449–1452.
[18] Z. Peng, H. Yin, Y. Yao, S. Chen, Effect of thin-film length on the peeling behavior of film-substrate interfaces, Phys. Rev. E 100 (2019) 032804.
[19] X. Yuan, P. Zhao, Q. Fan, The peeling behavior of compliant nano-films in adhesive contact with a planar rigid substrate: insights from molecular dynamics and continuum mechanics, Thin-Walled Struct. 204 (2024) 112272.
[20] Z.L. Peng, S.H. Chen, Effect of bending stiffness on the peeling behavior of an elastic thin film on a rigid substrate, Phys. Rev. E 91 (2015) 042401.
[21] S.M. Xia, L. Ponson, G. Ravichandran, K. Bhattacharya, Adhesion of heterogeneous thin films-I: elastic heterogeneity, J. Mech. Phys. Solids 61 (2013) 838–851.
[22] H.B. Yin, Z.L. Peng, S.H. Chen, The peeling behavior of a heterogeneous elastic film on a rigid substrate, Int. J. Solids Struct. 285 (2023) 112529.
[23] C.-S. Shen, H.-F. Wang, F. Yao, B. Li, B. Zhou, X.-N. Zhao, et al., Multiple kinds of peeling processes and instabilities in heterogeneous film peeling, Int. J. Solids Struct. 282 (2023) 112468.
[24] A. Ghareeb, A. Elbanna, Adhesion asymmetry in peeling of thin films with homogeneous material properties: a geometry-inspired design paradigm, J. Appl. Mech.-T Asme 86 (2019) 071005.
[25] R. Garg, N.V. Datla, Peeling of heterogeneous thin films: effect of bending stiffness, adhesion energy, and level of heterogeneity, J. Adhes. 95 (2018) 169–186.
[26] B. Chen, P. Wu, H. Gao, Pre-tension generates strongly reversible adhesion of a spatula pad on substrate, J. R. Soc. Interface 6 (2008) 529–537.
[27] B. Chen, X. Shi, H. Gao, Apparent fracture/adhesion energy of interfaces with periodic cohesive interactions, Proc. R. Soc. A: Math. Phys. Eng. Sci. 464 (2007) 657–671.
[28] L. Avellar, T. Reese, K. Bhattacharya, G. Ravichandran, Effect of cohesive zone size on peeling of heterogeneous adhesive tape, J. Appl. Mech.-T Asme 85 (2018) 121005.
[29] H. Yin, Z. Peng, Y. Yao, S. Chen, H. Gao, A general solution to the maximum detachment force in thin film peeling, Int. J. Solids Struct. 242 (2022) 111546.
[30] K. Kendall, Control of cracks by interfaces in composites, Proc. R. Soc. A: Math. Phys. Eng. Sci. 341 (1975) 409–428.
[31] N.W. Rizzo, K.H. Gardner, D.J. Walls, N.M. Keiper-Hrynko, T.S. Ganzke, D. L. Hallahan, Characterization of the structure and composition of gecko adhesive setae, J. R. Soc. Interface 3 (2006) 441–451.
[32] B. Ameri, M. Moradi, B. Mohammadi, D. Salimi-Majd, Investigation of nonlinear post-buckling delamination in curved laminated composite panels via cohesive zone model, Thin-Walled Struct. 154 (2020) 106797.
[33] P.W. Harper, S.R. Hallett, Cohesive zone length in numerical simulations of composite delamination, Eng. Fract. Mech. 75 (2008) 4774–4792.
[34] A. Turon, C.G. Dávila, P.P. Camanho, J. Costa, An engineering solution for mesh size effects in the simulation of delamination using cohesive zone models, Eng. Fract. Mech. 74 (2007) 1665–1682.